



5

Structure/Property relations in PVD hard coatings

P.H. Mayrhofer and C. Mitterer

Department of Physical Metallurgy and Materials Testing, and Materials Center Leoben
University of Leoben, Franz-Josef-Strasse 18, A-8700 Leoben, Austria

Abstract

Hard coatings deposited by Physical Vapor Deposition (PVD) based on the transition element nitrides are nowadays widely applied to reduce wear and corrosion of tools. In the last two decades, tremendous advances have been achieved in the development of deposition and application technology of hard coatings. The methods to be applied to optimize coating properties are known from materials science, however, only in the last few years significant attempts have been made to use them for designing coatings showing the properties required. The aim of this paper is to show the interrelationships between microstructural parameters like grain size or stress and mechanical coating properties and thermal stability. This is demonstrated using conventional coating systems like TiN and CrN as well as nanocomposite coating systems like TiN-TiB₂ and TiC-TiB₂. To interpret the interrelationships between processing, microstructure and mechanical and thermal properties, the well known fundamentals of materials science are used.

1. Introduction

The modern methods of plasma-assisted PVD techniques provide great flexibility for designing materials chemistry and microstructure, leading to coatings with improved or even unique properties. Starting with TiN in the early 70-ies [1], the stable solid solution Ti(C,N) (where carbon is added at the expense of nitrogen) was developed to enhance abrasion and erosion resistance. In the middle of the 80-ies, (Ti,Al)N has been successfully introduced where Al is incorporated in the TiN lattice forming a metastable solid solution [2]. The formation of a dense adherent aluminum oxide layer on top of the hard coating during high temperature applications (above 650°C) results in a significantly improved oxidation resistance [3] and enables machining with reduced coolant or even dry cutting [4]. Very recently, it has been shown that the high-temperature behavior can be improved further by adding small amounts of Y and Si (which also form stable oxides) to (Ti,Al)N [5]. For applications where the tool is applied under tribological and corrosive loads, CrN which shows an increased corrosion resistance is the standard choice [6].

In the last few years, several other hard coating materials with unique properties have been developed or even transferred to industrial applications. Essentially, two different coating material groups can be distinguished. The first one includes materials with inherent unique properties, e.g., diamond-like carbon DLC [7], diamond [8] and cubic boron nitride [9] as inherently hard or even superhard (where the hardness exceeds 40 GPa) materials or aluminum oxide as thermally extremely stable coating [10]. The second group covers heterostructures. Unlike the multilayer coatings like the commercially applied TiC-Al₂O₃-TiN coatings deposited by CVD techniques with layer thicknesses in the order of a few to several tenth of microns [11], nanoscaled heterostructures allow the design of unique properties or property combinations. The first attempts to deposit these structures have been made with the goals (1) to create new superhard materials (see e.g., the recent review by Vepřek [12]) or to combine properties like high hardness with (2) high toughness [13] or (3) a low friction coefficient [14,15]. The latter task focuses on the design of functional coatings where nanodispersive structures consisting of hard (e.g., TiN) and lubricant phases (e.g., DLC, MoS₂) have been suggested. Here, this topic will not be discussed further.

In this review, we will summarize the present status of research and technological development in the field of optimization of mechanical properties and thermal stability of hard coatings. We will start with a brief summary on the possibilities to influence coating microstructure by growth parameters. The main part of the paper is focused on the interrelationships between coating microstructure and their mechanical properties and thermal stability. These interrelationships will be demonstrated using several coating materials investigated in the authors' laboratory. To take care of the grain boundary structure, investigations were done with single phase (TiN, CrN), dual-phase (CrN-Cr₂N) and nanocomposite (Ti-B-N, Ti-B-C) hard coatings. The sputtering technique was chosen for deposition as a consequence of the unmatched versatility in obtaining different coating materials. Furthermore, by using unbalanced magnetron sputtering equipped with an external Helmholtz coil system, this deposition technique offers the possibility of a defined ion bombardment of the growing films. The ion bombardment, characterized by the ion energy (E_i) and the ion/atom flux ratio (J_i/J_a), has been identified as a useful tool to tailor coating microstructure and properties.

2. Structure and morphology

Hard coatings based on nitrides, carbides, borides and oxides may be deposited using Chemical Vapor Deposition (CVD) or Physical Vapor Deposition (PVD). Due to the high temperatures used, CVD coatings usually are in thermodynamic equilibrium [16]. Plasma-assisted PVD (PAPVD) or CVD (PACVD) processes use low-pressure discharges and offer thus the ability to synthesize materials far from thermodynamic equilibrium [17,18] which is attractive for research and processing of new materials. However, to use these methods for the design of coatings with improved properties, a detailed knowledge of the characteristics of the deposition process is necessary.

For e.g., sputtering, the following species are contributing to activate film growth: The number and the energy of film-forming atoms sputtered from the target depends on the energy and the number of the inert gas ions impinging at the target surface, and the sputtering yield for the combination of elements chosen. During the sputtering event at the target, inert gas ions may be reflected as energetic atoms due to elastic collisions with target atoms [19]. The ion energy and ion flux density at the substrate are often controlled by the substrate bias potential, however, other external parameters like total pressure and target current influence these values, too. Furthermore, the ion flux density may be controlled directly via an externally applied axial magnetic field using unbalanced magnetrons [20]. Plasma radiation is assumed to play only a minor role in supplying energy to the growing film [21].

Using growth-related deposition parameters instead of system-depending process parameters is highly suitable to compare properties of coatings deposited in different deposition plants. Moreover, the detailed knowledge of the interrelationships between growth parameters and resulting coating microstructure provides an excellent basis for designing coating microstructure according to the specific requirements. The well known influence of deposition parameters on the microstructure of coatings is a topic of numerous publications. According to Thornton's structure-zone model (SZM) the porous, tapered crystallites of TiN separated by voids which correspond to zone 1 can be transformed into zone I by decreasing the total working pressure (p_T), as shown in for a decrease of p_T from 0.8 to 0.4 Pa [22]. By lowering p_T , the number of collisions between sputtered atoms and working gas is reduced (i.e., the mean free path increases). This causes the sputtered atoms to arrive at the substrate surface with higher kinetic energy. Also, the adsorption of argon atoms from the sputtering atmosphere at the film surface might decrease, which is assumed to increase the surface mobility of coating adatoms. Using a more intense ion bombardment, the variation in working gas pressure, as a consequence of decreasing adsorption does not show this distinct influence. To lower the surface energy, especially at mild ion bombardment conditions, facets are created (Fig. 1). Increasing the ion bombardment causes a transition from the columnar to a dense, almost equiaxed structure. This behavior follows the revised SZM by Messier et al. [23]. Increasing ion bombardment during deposition (1) increases the nucleation density by forming additional nucleation sites (defects, implanted and recoil-implanted species), (2) increases the surface mobility of adatoms, (3) decreases the formation of interfacial voids and (4) by introducing thermal energy directly into the surface region promotes reaction and diffusion [24]. These effects are responsible for the formation of fine grained zone I structures or almost equiaxed grains having a smooth surface.

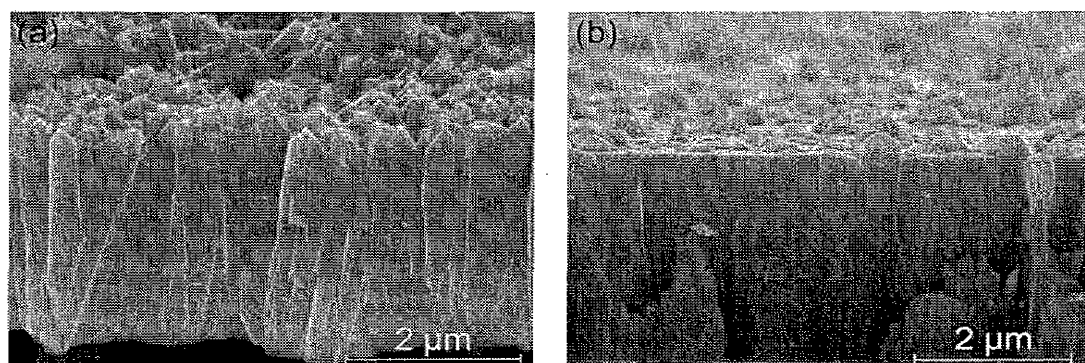


Figure 1. Scanning electron microscope (SEM) fracture cross sections of non-reactively sputtered TiN coatings (a) $p_T = 0.8$ Pa, (b) $p_T = 0.4$ Pa.

Especially single phase coatings (e.g., TiN, see Fig.1 and CrN) show a distinct dependence of their structure on the ion bombardment during deposition. This is valid for both non-reactive and reactive deposition. The transition from a pronounced columnar growth to a fibrous, dense microstructure occurs for non-reactive sputtering at milder ion bombardment conditions compared to the reactive deposition [25]. If a coating consists of more than one phase there is a competition during the growth of these phases. Consequently, these coatings show a denser and almost equiaxed microstructure even at mild ion bombardment conditions as compared to the single phase coatings [26]. Fig. 2a shows a fracture cross section of a $\text{CrN}_{0.65}$ coating which consists of the CrN and the Cr_2N phase. The competitive growth is highly effective if the growing phases show different preferred growth directions. This is often valid if the phases show different lattice structures (e.g., fcc, TiN, TiC, CrN; cph, Cr_2N , TiB_2) and therefore, different favorable orientations. Different growth directions are also valid for single phase coatings at the very beginning of the deposition. Starting from randomly oriented nuclei, these coatings show dense and equiaxed grains, which can often be observed at the vicinity to the substrate [27]. However, as a consequence of preferred growth directions there is a transition to columnar growth, depending on the ion bombardment. The more the growing phases interfere, the more dense and fine grained coatings are formed. In the nanocomposite coatings Ti-B-N and Ti-B-C there is a competitive growth between the phases TiB_2 and TiN or TiC, respectively [28-30]. Therefore, even at a mild ion bombardment these coatings show a dense, equiaxed and nanocrystalline structure. Figure 2b shows a completely featureless microstructure, which is typical for nanocomposite coatings.

The X-ray diffraction (XRD) analyses of non-reactively and reactively deposited TiN coatings [30] show a change in orientation from an almost random orientation over a preferred (110) to a pronounced (111) orientation by increasing the ion bombardment during deposition. Reactively sputtered CrN coatings also show this tendency of an orientation change from a preferred (100) through a (110) to a preferred (111) orientation by increasing the ion bombardment (cf. Fig. 3a) shows the importance of both parameters (E_i , J_i/J_a) for this orientation change. A change in orientation from a preferred (100) to a (110) orientation can be achieved by increasing E_i at constant J_i/J_a and vice versa. If there is a significant increase of J_i/J_a , this change occurs even by lowering E_i and conversely.

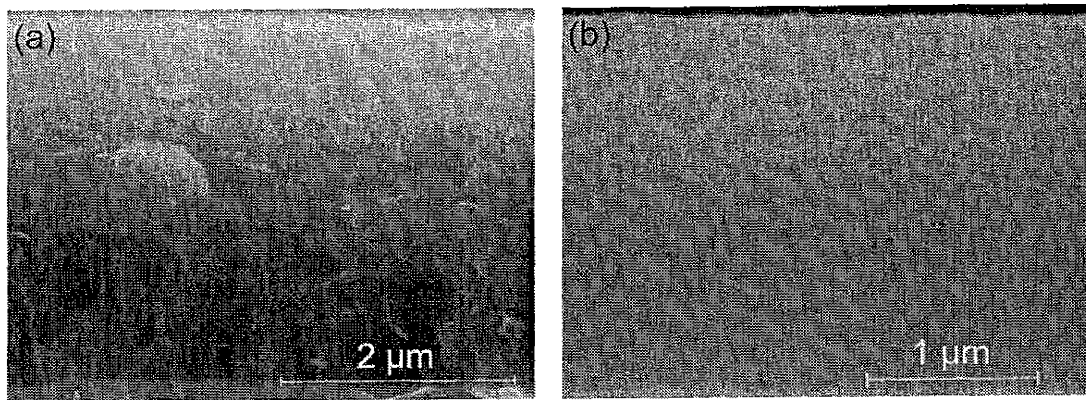


Figure 2. SEM fracture cross-sections of a (a) reactively sputtered $\text{Cr}_{1.5}\text{N}$ and a (b) non-reactively co-sputtered $\text{TiB}_{0.55}\text{N}_{0.95}$ coating.

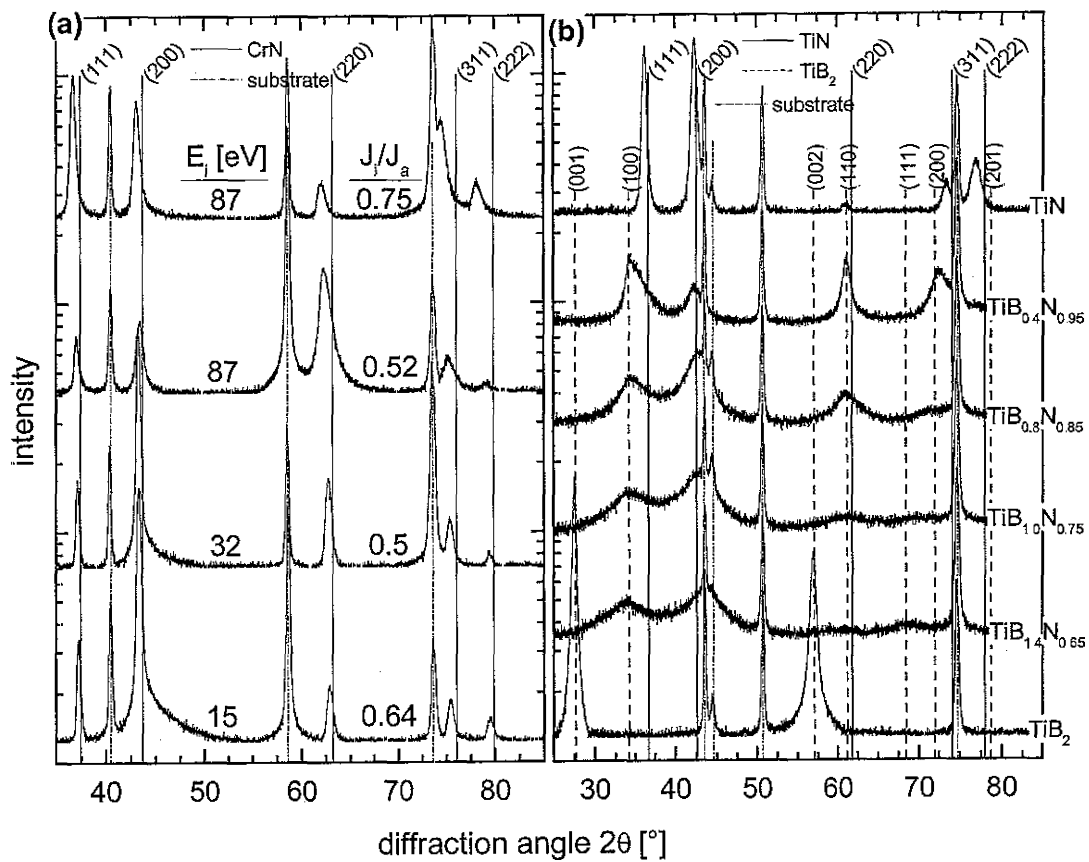


Figure 3. XRD patterns of (a) stoichiometric CrN films on a Mo substrate as a function of the ion bombardment during deposition and (b) Ti-B-N on a stainless steel substrate as a function of their chemical composition.

If the surface mobility is sufficiently high, lowering the surface energy determines the development of a preferential orientation in a coating [31]. TiN and CrN have a B1-NaCl crystallographic structure, where the (100) plane is the closest-packed surface and consists of either all Ti, Cr or all N atoms. These materials show a succession of increasing surface energy for the (100), (110) and (111) lattice planes, respectively [32,33]. Also, the activation energy for adatom formation and surface diffusion is lower for the (100) than for the (111) plane [34]. Thus, there should be a change in orientation from preferred (111) to (100) by increasing the ion bombardment, because of the increasing surface mobility of the adatoms. This behavior is valid for surface energy controlled growth and was found by many authors [31,35,36]. The transition to a preferred orientation with increasing ion energy is also a result of the anisotropy in the collision cascades. In channeling directions, where the energy of the impinging ions is distributed over larger volumes, lattice planes will be less distorted. This in turn, implies that planes corresponding to easy channeling directions and lower sputtering yields will have the highest probability of surviving. At normal incidence, the TiN or CrN [111] direction exposes a dense array of atoms to the ion bombardment direction and [100] and [110] are the most open channeling directions. Therefore, these directions are favored for penetration of argon at high values of E_i . Consequently, re-sputtering, which is valid at high energetic ion bombardment is less effective for the (100) and (110) planes [37-39]. Thus, again a (100) preferred orientation should develop with increasing ion energy. Under much higher intensity of the ion bombardment and low energy these effects are, however, overshadowed by ion-induced damage production returning the system to a (111) preferred orientation. Therefore, low energetic ion bombardment ($E_i \leq 120$ eV), which is valid for all coatings investigated in this work, results in a (111) growth-controlled orientation [31,40].

In general, the preferred orientation of a coating will be determined by the lowest overall energy conditions resulting from a critical competition between the strain and surface energies. It is supposed that TiN and CrN as a consequence of their B1-NaCl structure show orientation-depending elastic properties. The Young's moduli decrease in the sequence of E_{100} , E_{110} and E_{111} [32]. Therefore, it is expected that the strain energy term will be higher for (100) than for (110) and (111) orientations. Thus, a (111) orientation is preferred. This behavior was found in the present work and in many other publications [31,34,36,41-43]. Whereas the surface energy is independent of the coating thickness, the strain energy increases linearly with coating thickness [32]. Therefore, at small coating thickness the surface energy might be significant and a (100) orientation can be expected. At higher thickness, the strain energy difference between the corresponding directions becomes dominant and a (111) or (110) preferred orientation is favored [32,42]. Besides the discussed effects also the composition of gas mixture, working gas pressure and of course the deposition technique influence the development of a preferred orientation. Consequently, many different results are obvious.

Fig. 3b shows the development of XRD patterns of nanocomposite Ti-B-N coatings as a function of the chemical composition compared to their single phase coatings TiN and TiB₂. It seems that these nanocomposite coatings show a preferred (100) orientation for both crystallographic phases (TiN and TiB₂). These findings were also obtained from GAXRD patterns [30]. However, due to the broad and small peaks the main result of the XRD (Fig. 3b) and GAXRD [30] patterns is that the peak width decreases with

decreasing TiB_2 content. Since broadening of XRD peaks is caused by increasing microstresses and decreasing grain size, a decreasing grain size with increasing TiB_2 content is expected.

Summing up the results obtained for different hard coatings, it can be concluded that strictly applying growth parameters describing the number and energy of species impinging at the film surface should offer the possibility to directly compare interrelationships between process conditions for different deposition plants and the resulting microstructure and properties of coatings [37].

3. Interrelationships between microstructure and mechanical properties

The science of materials is to a large extent couched in terms of length scales and their interactions. The mechanical response of materials can be understood from the point of view of the interaction of a characteristic length, which may be the dislocation radius at a given stress, with a size parameter describing the microstructure (e.g., grain or particle size, film thickness) [44]. Strengthening of polycrystalline materials by grain size refinement is technologically attractive because it generally does not adversely affect ductility and toughness. The effect of smaller grain sizes on the yield stress is classically described by the Hall-Petch relationship which is based on dislocation pile-up at grain boundaries. This results in a dependence of the yield strength σ_y which is described by [45,46]

$$\sigma_y = \sigma_0 + k_{HP} \frac{1}{\sqrt{d}} \quad (1)$$

where σ_y and k_{HP} are constants and d is the grain size. Crystalline bulk materials usually follow Eq. 1 over several orders of magnitude in grain size. However, it is evident that the model behind the Hall-Petch relationship must break down for very small grains where dislocation plasticity is limited. This limit is given by the condition that at least one dislocation loop must fit into a grain [44,47]. As a simple approach, the comparison of the characteristic length, i.e., the diameter of the dislocation loop, with the relevant size parameter, i.e., the average grain size, determines the limit of validity of Eq. 1. As shown in Fig. 4a, this critical grain size (d_c) can be estimated to about 12 nm for sputtered CrN coatings with stoichiometric composition [48].

The mechanisms valid below this critical grain size are not fully clear. Several authors report on a softening for values below the critical one (see Fig. 4a or [44,47,48]) which is related to the so-called inverse Hall-Petch effect. There are several explanations for this behavior: Including the dislocation stress field, where the upper cut-off distance is supposed to equate the grain size in nanocrystalline materials, makes the radius of the dislocation loop sensitive to the grain size, as proposed by Arzt [44]. Shiøtz et al. [49] found that softening is mainly a result of grain boundary sliding where a few atoms undergo a large number of uncorrelated sliding events with respect to each other. In the grain interiors, only little dislocation activity is seen using atomic-scale simulations. The

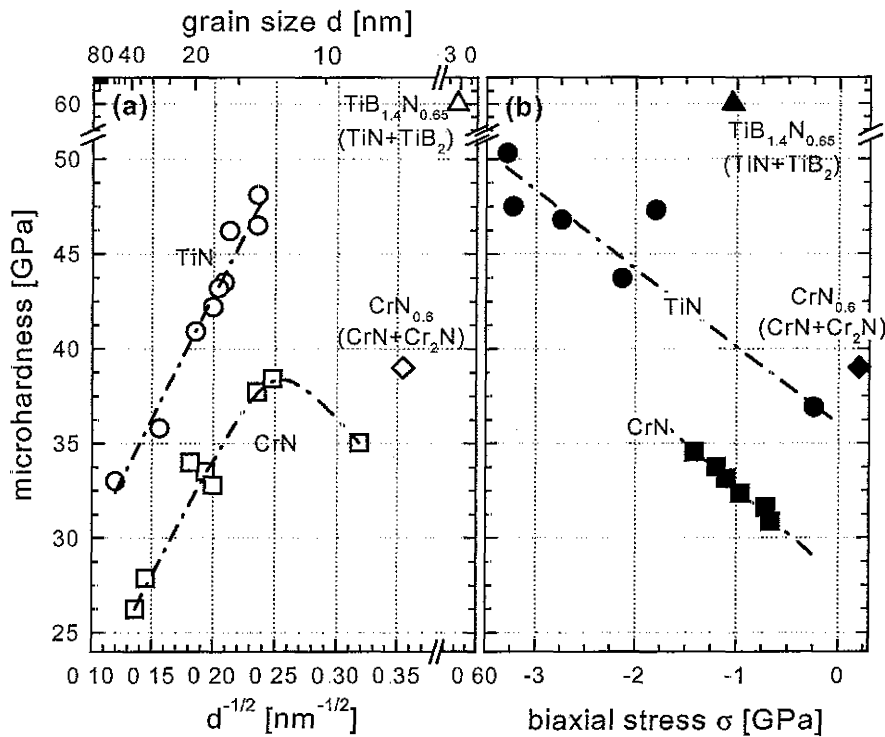


Figure 4. Interrelationships between (a) hardness and grain size and (b) hardness and biaxial coating stress for sputtered single-phase and dual-phase hard coatings [25,48].

localization of the deformation to the grain boundaries leads to a hardening effect as the grain size is increased. Summing up, a transition from dislocation-dominated plastic deformation to grain boundary sliding occurs at a critical grain size when the stress required for dislocation motion or formation becomes larger than for grain boundary sliding. As shown in Fig. 4a, this transition corresponds to a maximum in hardness of stoichiometric CrN, where coating microstresses close to zero are observed [48]. It should be noted that those single-phase coatings (CrN, TiN) which do not follow the Hall-Petch relationship shown in Fig. 4a show an excellent correlation between their hardness and microstress (see Fig. 4b).

For reactively and non-reactively sputtered TiN coatings which follow the HPR, the highest hardness values could be obtained for those coatings showing the smallest grain size. Contrary to these findings, the highest hardness for stoichiometric CrN coatings was not related to the smallest grain size. This is the result of the mentioned inverse Hall-Petch effect for a grain size below the critical one, as discussed before [48]. Otherwise, if the neighboring grains are of different lattice structures and therefore of different slip systems, it becomes much more difficult for dislocations to run through several grains. Thus, a CrN_{0.6} coating, which consists of the CrN (fcc, number of possible slip systems: 12) and the Cr₂N (cph, number of possible slip systems: 3) phase shows even at the grain size of 8 nm, which is smaller than d_c obtained for stoichiometric CrN, an extremely high hardness of 39 GPa even for tensile residual stresses (see Fig. 4a) [48,50].

Based on the mechanisms described before, the concept of superhard multilayer coatings, i.e., superlattices, was introduced in the end of the 80-ies using bilayer repeat periods in the order of about 10 nm [51]. Maximum hardness values have been reported for TiN/VN [52] and TiN/NbN [53] with values exceeding 50 GPa which is more than double the hardness of either component of the multilayer coating. Barnett and co-workers found that there is a hardness increase when the elastic moduli of the two nitrides involved are different, thus explaining why no significantly higher hardness was found for NbN/VN [54]. This is one successful example of the design of hard coatings driven by materials science: Superlattices based on CrN/NbN or (Ti,Al)N/CrN can nowadays be deposited on an industrial scale using the combined steered arc evaporation and closed-field unbalanced magnetron sputtering, where the thickness of the individual layers is controlled by altering the substrate rotation and the deposition rate for the different targets used [55].

In 1995, Vepřek and co-workers [56] presented their model on the design of novel superhard nanocomposite coating materials. Using PACVD, they deposited coatings within the system TiN-Si₃N₄ and achieved superhardness values of 80 to 105 GPa [57]. The superhardness observed was explained by a generic concept based on hindered dislocation movement and grain boundary sliding as well as the low crack size possible [58]. Following the assumption of limited plasticity of these materials, Vepřek suggested to use the well-known Griffith criterion for describing the mechanical behavior of nanocrystalline coatings [59]:

$$\sigma_c = \sqrt{\frac{2}{\pi} \frac{E\gamma_s}{a_c}} \quad (2)$$

where σ_c is the critical stress required for crack propagation in brittle materials, E is the elastic modulus, γ_s is the specific surface energy and a_c is half the length of an internal crack. Assuming that the crack is formed in the grain boundary region which consists of a softer quasi-amorphous phase, the maximum crack length is assumed to be in the order of a few nm, when crack propagation is stopped at well-defined sharp interfaces. Using this approach, it is possible to extend the validity of the Hall-Petch relationship to smaller grain sizes and, consequently, reach the superhardness values reported.

During the last years, several other hard coating systems based on nanoscale composites have been proposed. Generally, two different groups can be distinguished, i.e., nanocomposites based on two hard phases [26,60] or on one hard and one soft phase [61,62]. The aim of these coating developments is to (1) achieve superhardness or (2) combined high hardness and ductility, respectively. Among others, superhardness values have been achieved using the coating systems TiN-TiB₂ (hardness up to 54 GPa [63]) or TiC-TiB₂ (hardness up to 71 GPa [60]). The development of nanocomposite coatings consisting of one hard and one soft phase is directed towards the improvement of the wear resistance of engineering components where mild steels or light alloys (with low elastic moduli) are commonly used. Nanocomposites consisting e.g., of a supersaturated Cr(N) solid solution or ZrN (both providing a suitable hardness) and the low-miscibility metal Cu (which surrounds the hard nanoparticles as a minority matrix phase [64]) provide the potential to design coatings with a hardness similar to that of superhard coatings but allow the retention of elastic properties close to that of the softer substrate

material. For example, for ZrN-Cu nanocomposite coatings, hardness values in the range of 22-50 GPa and elastic moduli between 215 and 380 GPa have recently been reported [64]. This gives rise to design coatings with reasonable hardness and elastic properties close to those of the alloys used in engineering. For example, a single-phase TiN coating shows a hardness of about 35 GPa and a reduced elastic modulus of 380 GPa. Using a nanocomposite TiN-TiB₂ coating and comparable deposition conditions, a high hardness of 52 GPa and a low elastic modulus of 325 GPa have been obtained.

The nanocomposite coatings Ti-B-N and Ti-B-C consist of two different nanocrystalline phases TiB₂ (cph) and TiN (fcc) or TiC (fcc), respectively. Since in nanocrystalline materials the deformation mechanism changes from dislocation nucleation and motion to small-scale sliding in the grain boundaries (from an intragranular to an intergranular process, from bulk to interface), the consistence of the grain or phase boundaries is highly important. Whereas in Ti-B-N coatings d_c seems to be about 3 nm, in Ti-B-C the highest hardness could be obtained for the coating having also the smallest grain size of 2 nm [60].

Lowering the total working gas pressure during non-reactive co-sputtering of Ti-B-N coatings from 0.8 to 0.4 Pa yielded an increase of their hardness even at lower ion energies (cf. Fig. 5a). The Ti-B-N coatings deposited at $p_T = 0.4$ Pa show grain sizes of about 2.5 nm, those deposited at $p_T = 0.8$ Pa vary between 2 and 6 nm depending on their chemical composition [60]. As a consequence of the extremely broad peaks of the nanocomposite Ti-B-N coatings, an exact determination of the grain size is difficult. However, using the succession of decreasing peak width with decreasing boron content in the coatings (cf. Fig. 3b) the assumption of an increasing grain size is justified, as discussed before. The single phase coatings TiB₂ and TiN show nearly the same microhardness values for the two different deposition series (see Fig. 5a). However, these hardness values could be obtained for the lower working gas pressure of 0.4 Pa at a much lower ion energy of 25 eV, compared to $E_i = 87$ eV at $p_T = 0.8$ Pa. This is mainly a result of the densification of the microstructure of coatings by lowering the total working gas pressure (cf. Fig. 1). The grain sizes of TiB₂ and TiN (deposited at $p_T = 0.4$ Pa) could be calculated from XRD line broadening [50,65-67] to 22 and 41 nm, respectively. The microhardness of the TiN coating fits exactly the HPR of non-reactively sputtered TiN coatings, which were deposited using the same total working gas pressure of 0.4 Pa [25]. As it is obtained for the single phase coatings, a densification of the microstructure for the nanocomposite coatings by lowering the working gas pressure is also expected. Therefore, the hardness values for Ti-B-N coatings are comparable for the deposition series using a p_T of 0.4 and 0.8 Pa, respectively even if the ion energy is much lower.

Although the microhardness is comparable for these two deposition series, the reduced elastic moduli show completely different values for the single-phase as well as for the nanocomposite coatings (cf. Fig. 5b). Since in nanocrystalline materials a large volume fraction of atoms belong to the grain boundary, their Young's modulus decreases as the grain size decreases. This is because grain boundaries have a lower Young's modulus compared to the neighboring crystals. Therefore, the microstructure of the grain boundaries or phase boundaries plays an important role in nanocrystalline or nanocomposite coatings. The Young's modulus also decreases as the porosity of a sample increases, but this implies also a decrease in hardness [49,68]. However, the

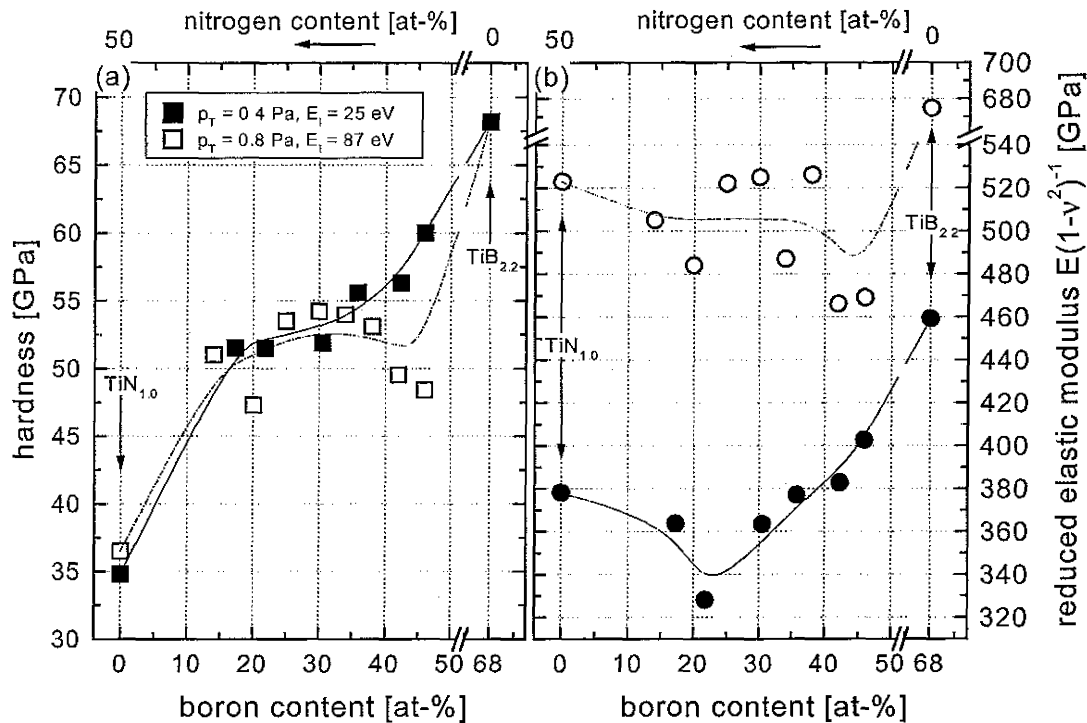


Figure 5. (a) Hardness and (b) reduced elastic modulus of Ti-B-N coatings as a function of their chemical composition depending on the total working gas pressure (p_T).

coatings investigated show even higher hardness values combined with lower Young's moduli (cf. Fig. 5). This behavior excludes that increasing porosity is reasonable for the lower Young's moduli. On the contrary, decreasing the total working gas pressure p_T combined with lower ion energy would result in a more dense microstructure as discussed before. Therefore, the most reliable explanation for higher hardness and lower elastic modulus is the smaller grain size and the improved formation of the grain and phase boundary region of the single phase and nanocomposite coatings. This is also emphasized by annealing experiments on stoichiometric TiN coatings [25]. After annealing, these coatings show lower micro- and macrostresses, lower dislocation density and larger grains due to recovery effects. It is also supposed that the excess of point defects anneal out during a heat treatment up to 700°C. These coatings show lower hardness values but somewhat higher Young's moduli (+ ~15 GPa) after the heat treatment. The increased grain size and reduced dislocation density are supposed to be mainly responsible for this behavior, however, not the reduced porosity of the samples.

Coatings having low elastic moduli (i.e., enhanced elasticity) and high hardness are favorable for many mechanical applications as reported in the literature [26,61,69-72]. It has been shown that using a H/E ratio instead of hardness alone has some merit in describing coating properties. It is beneficial for practical applications if the elastic modulus of a coating is close to that of the substrate used, which in turn, implies a reduction of the Young's moduli of hard ceramic coatings, since these are usually two or three times higher than those of the substrate material (e.g., steel) [62].

4. Interrelationships between microstructure and thermal stability

By plasma assisted deposition of hard coatings, thermodynamically unstable microstructures containing dislocations, subgrains and different kinds of point defects (Schottky, Frenkel) according to the ion bombardment conditions used are produced. Coatings may lower their stored energy by microstructural rearrangements [73-83], especially if a driving force in form of heating is added. The term thermal stability covers phenomena like recovery, grain growth, recrystallization, oxidation and - in the case of metastable pseudo-binary coatings - decomposition. They are essential in applications where the coating is subjected to high temperatures, e.g., in machining or die-casting [74], because they are usually accompanied by changes in coating properties.

4.1 Recovery

Recovery involves all annealing phenomena that occur before the appearance of new strain-free grains, i.e., migration and combination of point defects, rearrangement and annihilation of dislocations, growth and coalescence of subgrains [75]. Thus, the investigation of recovery effects is often done by stress measurements at elevated temperatures [76]. Fig. 6 shows an example of such biaxial stress temperature measurements (BSTM) [50] for a $\text{TiB}_{0.6}\text{N}_{0.7}$ coating deposited onto silicon substrates using different ion bombardment conditions. During heating of the film-substrate composite, the compressive stresses increase because of the higher thermal expansion coefficient of the $\text{TiB}_{0.6}\text{N}_{0.7}$ film with respect to the silicon substrate. In coatings having tensile stresses at room temperature, the heating first relaxes these tensile stresses and then eventually causes the film to go into a state of compression (cf. Fig. 6, the second run of the $\text{TiB}_{0.6}\text{N}_{0.7}$ coating deposited using a high ion energy). This thermoelastic behavior as a result of different thermal expansion coefficients between substrate ($\alpha_{\text{Silicon}} = 3.55 \cdot 10^{-6} \text{ K}^{-1}$) and coating ($\alpha_{\text{TiBN}} \sim 6-7 \cdot 10^{-6} \text{ K}^{-1}$ [30]) is only valid until recovery occurs. Further increasing the temperature results in a pronounced stress relaxation.

During the first heating cycle (shown in Fig. 6), the samples were also isothermally annealed for 1 h at the maximum temperature of 500°C. After that time of the isothermal annealing, no further change of the measured biaxial stresses could be observed. During the cooling segment the stress-temperature curve follows a straight line, again corresponding to the linear thermoelastic behavior. A second measurement immediately after the first one does not show any significant deviation of the heating segment from the cooling segment of the previous run, except for coatings showing cracks after the first stress-temperature cycle. Tensile cracks are formed during the cooling segment of the first run due to the high tensile stresses in the $\text{TiB}_{0.6}\text{N}_{0.7}$ coating deposited using a low energetic ion bombardment (cf. Fig. 6a). In this case the heating segment of the second stress-temperature curve deviates from the cooling segment of the previous one. As a consequence of the cracks in the coating also the slope of the stress-temperature curve is lower. However, for both coatings a deviation of the straight line during the heating portion of the second run appears only if the thermal activation is higher than the maximum of the first run. This is highly obvious for the coating deposited using a high energetic ion bombardment.

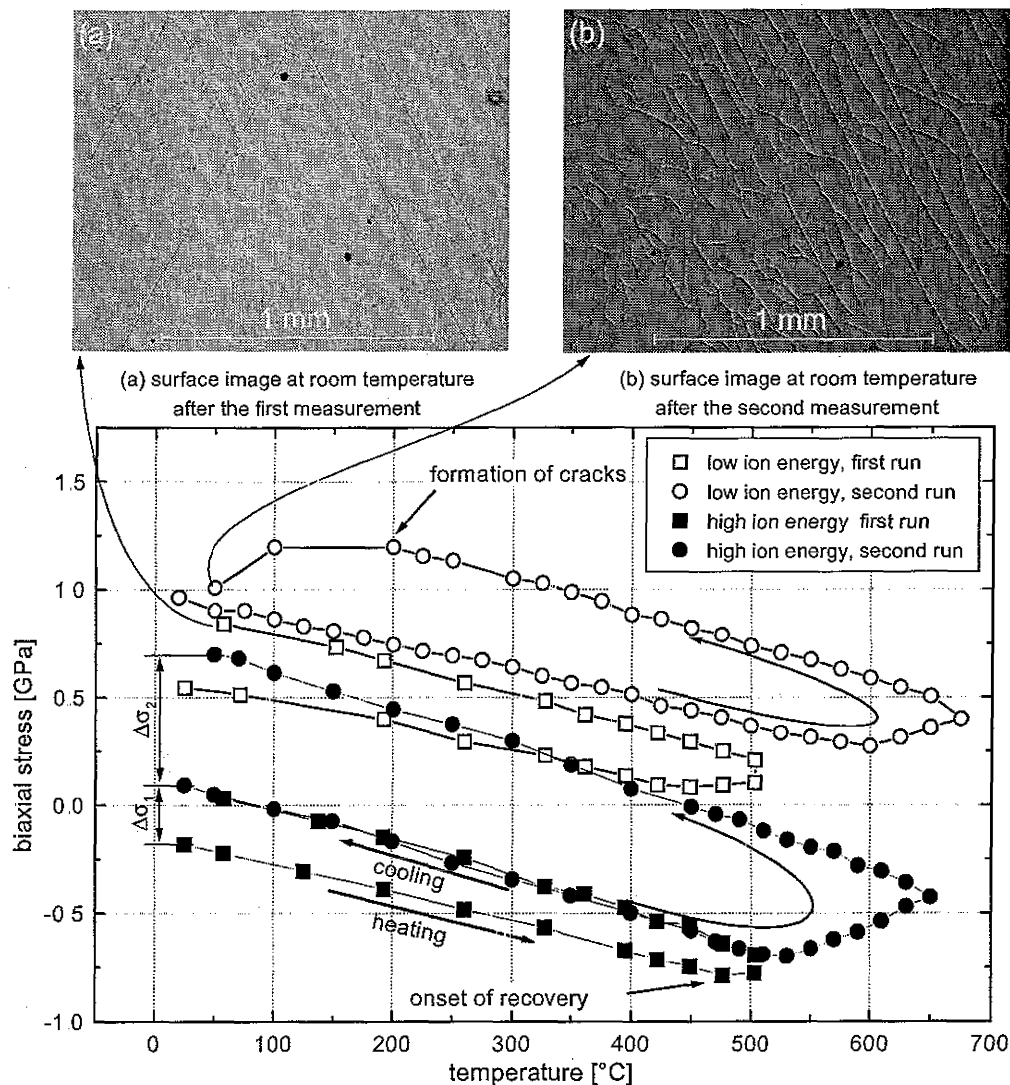


Figure 6. Stress-temperature cycles of a $\text{TiB}_{0.6}\text{N}_{0.7}$ coating deposited at low or high ion energy, respectively, for two different maximum temperatures, and corresponding light optical microscope surface images of the coating deposited with a low ion energy.

The second stress-temperature cycles, which were run up to a temperature of 650 or 675°C, respectively, indicates that most of the coating defects show a higher thermal stability than 500°C. There is no deviation of the cooling segment from the linear thermoelastic line, therefore, plastic deformation in the coating or substrate during this heat treatment can be excluded. A third run up to the same temperature as for the second one indicates also no deviation from the linear thermoelastic behavior and emphasizes again the different thermal stability of the different kinds of defects. But also the driving force (compressive stresses at elevated temperatures) decreases as recovery effects occur. This in turn also implies that higher thermal activation is needed to continue recovery. Therefore, stress-temperature cycles only show a deviation from the linear thermoelastic behavior if the thermal activation is higher than previous ones. A

pronounced formation of tensile cracks occurs during the cooling segment of the second stress-temperature cycle of the $\text{TiB}_{0.6}\text{N}_{0.7}$ coating deposited using a low ion energy. Therefore, the coating shows a pronounced deviation from the straight line during cooling. By comparing the surface images of the $\text{TiB}_{0.6}\text{N}_{0.7}$ coating before (Fig. 6a) and after the second stress-temperature cycle (Fig. 6b) the development of their tensile cracks is obvious.

If a coating shows compressive stresses (substitution and displacements of atoms on interstitial lattice sites, Frenkel pairs and Anti-Schottky defects), the recovery effects cause an obvious reduction of their stresses. However, intrinsic tensile stresses as a result of voids or vacancies (Schottky defects), which are promoted by a mild ion bombardment especially if the total working gas pressure is high, even increase during annealing. The thermal activation causes these defects to anneal out or move to grain boundaries which are favored places for lattice imperfections. This results in a decreasing coating volume and thus increases tensile stresses [84-86]. Fig. 6 shows, that the major part of stress relaxation occurs for temperatures higher than 500°C . Since the amount of stress relaxation is correlated to recovery of lattice defects, consequently most defects should have a thermal stability higher than 500°C .

Recovery of the different coating defects during annealing up to 700°C in vacuum is well discussed in previous papers for single phase (TiN, CrN) and nanocomposite coatings (Ti-B-N, Ti-B-C) [30,25,48]. It could be shown that for single phase coatings the thermal stability of the defects mentioned strongly depends on the residual biaxial stress in the as-deposited state. There is a linear dependence of the onset temperature for recovery as well as of the maximum stress relaxation ($\Delta\sigma$) which occurs during the heat treatment on the density of defects (as shown in Fig. 7b) [25,48]. This is valid for those single phase coatings showing a dense crystalline structure. Coatings showing a pronounced columnar growth deviate from this linear dependence because of the possibility of stress relaxation at open-voided grain boundaries [25]. This shows that for a stronger driving force (i.e., higher biaxial stress) a lower thermal activation is needed to start recovery. Also, the amount of recovery effects ($\Delta\sigma$) occurring during a heat treatment up to the same maximum temperature is directly related to the driving force [25,48]. As discussed in ref. [25], recovery effects of coatings contain, in addition to a better arrangement of point defects, also annihilation and rearrangement of dislocations into lower energy configurations. Especially if the coatings retain a high dislocation content, subgrain formation is promoted. On annealing, excess dislocations will arrange into lower energy configurations in the form of regular arrays or low angle grain boundaries (polygonization) [73,79,87]. The stored energy in a substructure is still large and can be further lowered by coarsening of the substructure. This leads to a reduction of the total area of low angle grain boundaries.

An increased grain size was found from XRD analyses and SEM fracture cross sections for the single phase coatings in the system Ti-N and Cr-N after annealing up to 700°C compared to those prior to annealing [25,48]. Especially coatings having small grain sizes prior to annealing show a more pronounced grain growth, due to the higher driving force (stored energy). It is also supposed that for single phase coatings, as a result of their grain boundary consistence, grain boundary sliding at elevated temperatures is more preferred than for nanocomposite coatings. This behavior can especially be seen from the BSIM for stoichiometric CrN coatings in Fig. 7a which

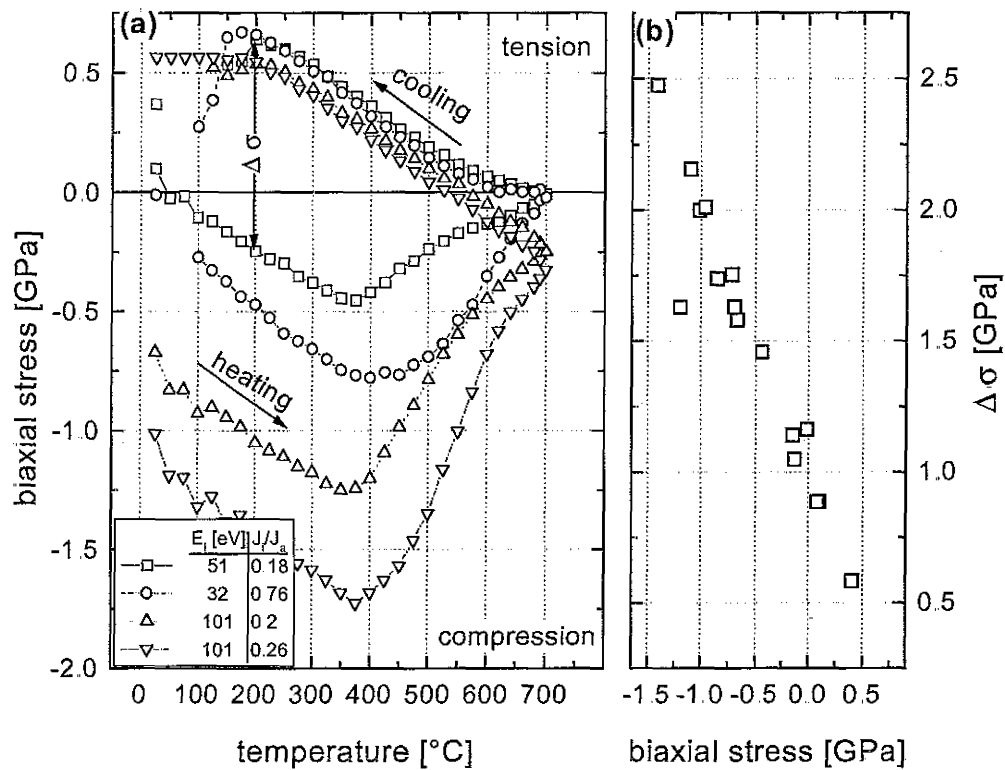


Figure 7. (a) Stress-temperature cycles for sputtered stoichiometric CrN coatings deposited onto silicon substrates and (b) influence of their biaxial stress in the as-deposited state on the stress relaxation during the heat treatment up to 700°C for different ion bombardment conditions (E_i , J_i/J_a)

reach the stress free state at the maximum temperature of 700°C [48]. The initial stress in the as-deposited condition can obviously be controlled through the ion bombardment during growth which creates lattice defects [77]. From the cooling segment, a deviation from the linear thermoelastic behavior is obvious at temperatures close to 700°C. The occurring grain boundary sliding and subgrain growth prevent an increase of tensile stresses during cooling as it would be if a linear thermoelastic behavior is present. If the temperature is below ~600°C, thermal activation is too low for these processes. Therefore, the stress-temperature curve of the cooling segment below 600°C shows a straight line, corresponding to the linear thermoelastic behavior [48].

In the nanocomposite coatings Ti-B-N and Ti-B-C, the thermal stability of the defects also strongly depends on the chemical composition. Coatings showing nearly the same amount of TiB₂ and TiN or TiC crystallites, respectively, which implies the highest amount of phase boundaries, also show the highest onset temperature for recovery [30]. These coatings have the smallest compressive stresses, which is related to stress relaxation during growth due to grain boundary sliding. In the nanocomposite coatings with a grain size of 2–6 nm, dislocations rapidly release to the grain boundaries. Consequently no subgrain growth can occur; the XRD patterns of Ti-B-N and Ti-B-C coatings after annealing look exactly like those prior to annealing. This indicates that no subgrain and grain growth occurred during an annealing treatment up to 700°C. Also,

microhardness values of these coatings after the heat treatment do not deviate from the previous ones. Or vice versa, as a result of the same grain size and microhardness values prior and after annealing it is supposed that there are no dislocations in these nanocomposite Ti-B-N and Ti-B-C coatings. Therefore, recovery effects in the nanocomposite coatings mainly concern annihilation and movement of point defects to lower their stored energy.

4.2 Recrystallization

Recovery, which was discussed in the previous section, is a relatively homogeneous process. In contrast, recrystallization involves the formation of new strain-free grains in certain parts of the specimen and the subsequent growth of these to consume the microstructure having defects. The microstructure at any time is divided into recrystallized or non-recrystallized regions, and the fraction recrystallized increases from 0 to 1 as the transformation proceeds. The kinetics of primary recrystallization are similar to those of a phase transformation which occurs by nucleation and growth. During recrystallization, nucleation corresponds to the first appearance of new grains in the microstructure and growth describes the replacement of the original grains by new ones. Recrystallization occurs if the thermal activation and driving force is sufficient. A detailed review on the recrystallization of hard coatings has been given recently by Hultman [77], who reported a relatively low stability against recrystallization for CrN at about 400-450°C (obviously, recovery is almost immediately followed by recrystallization in the case of CrN). For (Ti,Al)N coatings, annealing experiments at 900°C for 2 h yielded no observable recrystallization.

For superlattices or nanocomposite coatings, it is a major task to design coating structure in a way that recrystallization is hindered. Hultman et al. [88] estimated the lifetime of a TiN/NbN superlattice coating with an 8.3 nm periodicity to about 1 h at 900°C. For the system TiN-Si₃N₄, recrystallization and grain coarsening was observed for temperatures between 800 and 1200°C, where the recrystallization temperature showed an inverse relation to the grain size [57]. For the exact determination of the onset temperature for recrystallization (T_{rex}), differential scanning calorimetry (DSC) provides an excellent method. The driving force for recrystallization, which is the stored energy within the grains, comes from their defect density and grain size. Since in nanocomposite coatings essentially no dislocations are present, the main driving force is their grain size. The excess of point defects within the coatings are supposed to anneal to a high extent during recovery prior to recrystallization. Therefore, the thermal activation which is needed to initiate recrystallization strongly depends on the grain size besides the chemical composition of nanocomposite coatings [30].

For many conventional hard coatings, the energy released during recrystallization (transformation of high energetic microstructure into a low energetic one) is often too small to be detected by DSC. However, if the coatings show grain sizes in the nanometer region, the energy released during grain growth (ΔH), which occurs after recrystallization can be detected by DSC [89-92]. Therefore, during dynamical DSC investigations a heat flow (ΔH) at elevated temperatures could only be observed for nanocomposite coatings. For the single phase coatings, there is of course recrystallization and grain growth but no heat flow could be detected as a result of the small energy released by coatings having larger grains. The difficulties during dynamical

DSC measurements are related to the small total mass available of about 6 mg of the coatings investigated.

Fig. 8 shows an example of DSC investigations of nanocomposite coatings within the systems TiN-TiB₂ and TiC-TiB₂, where exothermic peaks can be observed in the temperature range between about 980 and 1090°C. These peaks correspond to a reduction of the interfacial energy. The heat release can be used to calculate the extent of grain coarsening. Starting from an average grain size of about 4 nm in the as-deposited state, the grain size after recrystallization yields values between 5 and 25 nm [30]. For both coating systems, grain growth is increasingly inhibited with increasing TiB₂ content. The values for the recrystallization temperature and the extent of grain coarsening show an excellent agreement with conventional annealing experiments and post-annealing investigation of the coating microstructure [25,30,93].

The recrystallization temperature (T_{rex}), which was found during dynamical DSC measurements using a heating rate of 50 K·min⁻¹ to be mainly a function of the chemical composition for Ti-B-N coatings, is 995°C for TiB_{1.2}N_{0.5} [30]. This was verified by SEM fracture cross section investigations of this coating after a heat treatment up to 950°C (Fig. 9a). This cross section shows a nearly featureless microstructure. Therefore, it can be assumed that essentially no grain growth takes place during a heat treatment up to 950°C, which emphasizes a higher T_{rex} . As for the influence of the total pressure during

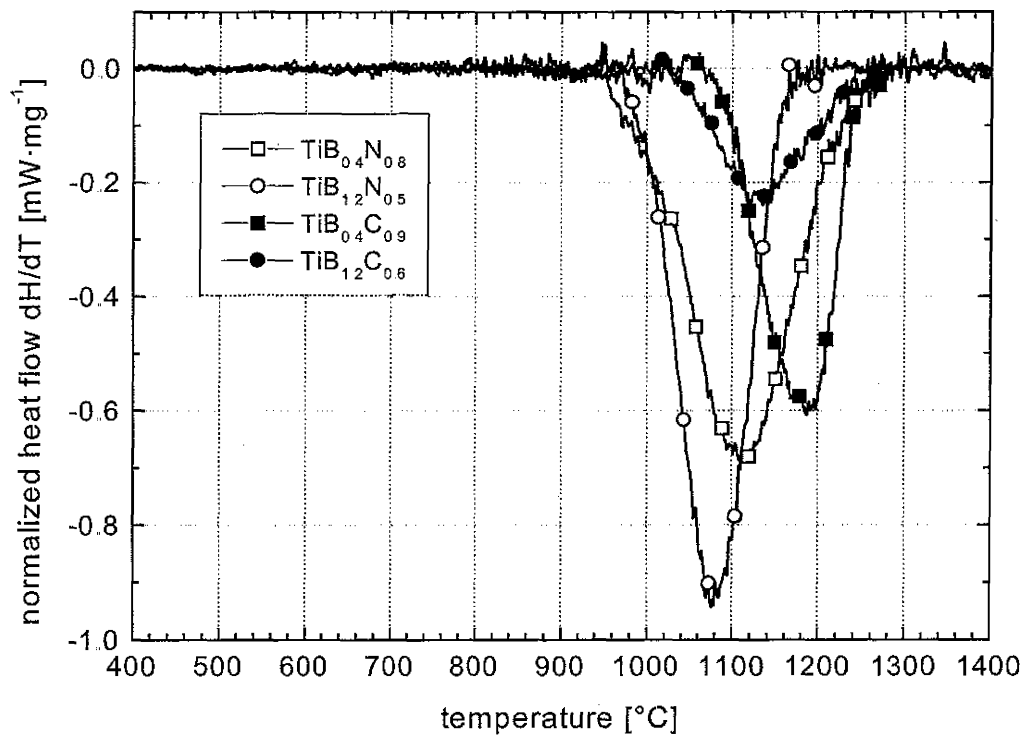


Figure 8. Dynamical DSC curves of nanocomposite Ti-B-N and Ti-B-C coatings recorded at a heating rate of 50 K min⁻¹ (for better legibility, symbols are given in the peak area for one out of 30 measurement points)

Table 1. Recrystallization temperature (T_{rex}), exothermic heat flow (ΔH) and activation energy for grain growth (Q_g) obtained by dynamical DSC measurements for Ti-B-N nanocomposite coatings deposited at different total working gas pressures showing different chemical composition.

Coating	T_{rex} [°C]	ΔH [J g ⁻¹]	Q_g [eV]	p_I [Pa]
TiB _{0.4} N _{0.8}	979	126	-	0.8
TiB _{1.2} N _{0.5}	995	110	-	0.8
TiB _{0.55} N _{0.95}	1032	59	7.9	0.4
TiB _{0.8} N _{0.85}	1047	115	6.9	0.4
TiB _{1.0} N _{0.75}	1054	126	6.4	0.4
TiB _{1.25} N _{0.7}	1070	161	4.4	0.4

deposition on the mechanical properties a pronounced increase of T_{rex} in the range of about 50°C higher temperatures could be obtained for a lower total pressure during deposition of 0.4 Pa (Table 1). This is supposed to be also a result of the denser microstructure (Figure 2b) and well defined grain and phase boundary structures, as discussed in the previous section. This is because vacancy mobility or supersaturation enhances the boundary migration, which in turn decreases T_{rex} [73,80,90-92].

Depending on the maximum temperature after the primary recrystallization also exaggerated grain growth can occur, which is often called secondary recrystallization or abnormal grain growth. This secondary recrystallization was obtained during a heat treatment up to 1400°C only for stoichiometric TiN (Fig 9b). The nanocomposite coatings did not show this abnormal grain growth during the same heat treatment. Fig. 9b shows that especially in the vicinity to the substrate exaggerated grain growth is obvious. The driving force for abnormal grain growth is also the reduction in grain boundary energy as for normal grain growth. An additional driving force, especially for thin coatings, arises from the orientation dependence of the surface energy [83,90]. Consequently, grains showing a (100) orientation should grow abnormally. Therefore, secondary recrystallization occurs for this TiN coating near the interface to the substrate due to the more uniform and denser microstructure, whereas the faceted columns belong to a (111) orientation.

The values of T_{rex} for all coatings investigated are in excellent agreement with the well known estimation for the onset of recrystallization (approximately 0.45 of the homologous temperature [73,79,80,87]). The coatings deposited at $p_I = 0.4$ and 0.8 Pa, respectively, show the same dependency of the recrystallization temperature on their chemical composition. Whereas T_{rex} shows different values for coatings showing a predominant TiN or TiB₂ phase, T_{rex} is similar for coatings having nearly the same amount of TiN and TiB₂ phases. This is reasonable for the discussed competitive influence of grain size and chemical composition on T_{rex} [30].

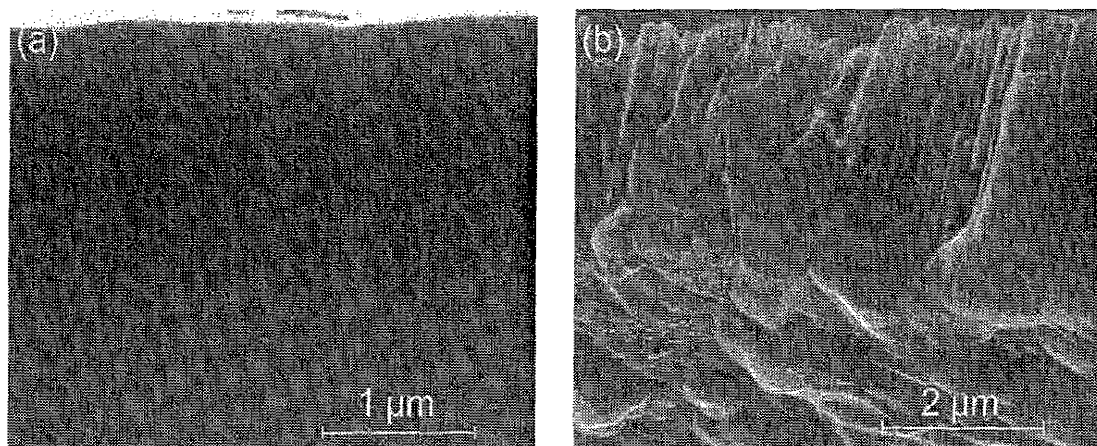


Figure 9. SEM fracture cross sections of (a) $\text{TiB}_{1.2}\text{N}_{0.5}$ coating after a heat treatment up to 950°C , (b) TiN coating after the dynamical DSC measurement up to 1400°C .

To determine the activation energy for grain growth (Q_g) occurring immediately after recrystallization by means of the Kissinger equation [94] (Eq. 3), different heating rates (B) during the DSC experiment are necessary.

$$\ln\left(\frac{B}{T^2}\right) = -\frac{Q_g}{R \cdot T} + \text{constant} \quad (3)$$

Here, R is the gas constant, and T a specific temperature such as the onset temperature T_o or the peak temperature T_p of the exothermic peak (due to grain growth). The onset temperature obtained during a DSC measurement using a heating rate of 50 K min^{-1} corresponds to T_{rex} . By using T_o or T_p values for the different heating rates, plots of $\ln(B \cdot T^2)$ vs. T^{-1} yield straight lines showing the same slope [95]. Fig. 10 shows the Kissinger plots for four different chemical compositions of Ti-B-N. The exothermic peak due to grain growth becomes more pronounced and is shifted to higher temperatures as the heating rate increases. From the slopes of these lines the activation energies listed in Table are obtained. The activation energy was found to increase with the TiN content (i.e., the nitrogen content) in the Ti-B-N coatings, whereas ΔH and T_{rex} decrease. It is reasonable that the activation energy needed for grain growth is higher for coatings having larger grains due to the smaller amount of stored energy and fewer nucleation sites [73,79-82,87]. This is emphasized also by the decreasing heat release (ΔH) with increasing grain size (i.e., higher nitrogen content) due to grain growth during the dynamical DSC measurement. However, similar to the findings for T_{rex} , the activation energies show very different values only for coatings having a predominant TiN or TiB_2 phase. This is supposed to be a reason of the competition between the chemical and grain size influence on the driving force for grain growth. But also the different bulk and surface diffusion for Ti, N and B in TiN, TiB_2 and their grain and phase boundaries, respectively, play major roles.

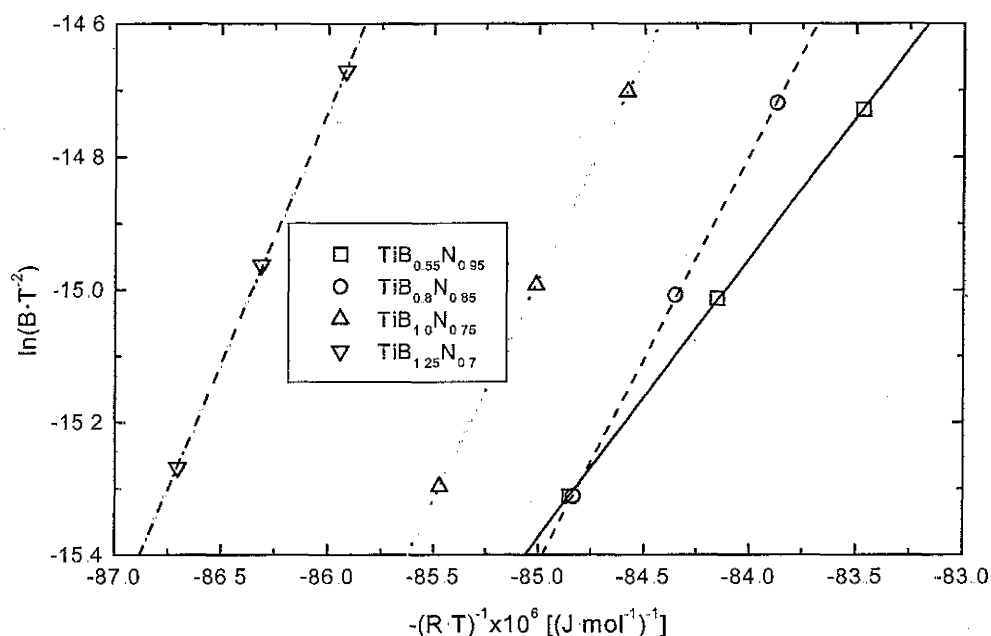


Figure 10. Kissinger plots of $\ln(B \cdot T^2)$ vs. T^{-1} for the exothermic peaks in the DSC curves using four different chemical compositions of Ti-B-N films

4.3 Oxidation

In general, oxidation describes a chemical reaction where an atom gives up one or more electrons (e^-) to form a positively charged ion. Reactions which consume e^- are called reductions. The term oxidation is used in for reactions involving oxygen. A metal (or metallic part of an intermetallic compound) reacts with oxygen to produce an oxide on the surface (metal + oxygen \rightarrow metal oxide). This section is about the system coating (metallic compounds like nitrides, carbides and borides of the transition metals), the formed oxide film and oxygen bearing gas at higher temperatures. Oxygen reacts readily with most metals, though the thermal energy required to produce significant oxidation rates may vary considerably for different materials at the same temperature. At ambient temperatures, most engineering materials are either already oxidized such that the oxide layer screens the underlying material from further reaction, or they react sufficiently slowly in dry air and in this case oxidation is not a real problem. At elevated temperatures, however, the rate of oxidation of metals increases [96-101].

The oxidation behavior was found for CrN coatings to be - besides their chemical composition - also a function of their microstructure and biaxial residual stresses [102]. The latter one strongly depend on the ion bombardment during deposition. The ion bombardment shows only a minor influence on the microstructure of the nanocomposite Ti-B-N and Ti-B-C coatings in the range investigated. Therefore, their oxidation is mainly influenced by their chemical composition. This was found during dynamical thermo-gravimetric analyses (TGA) of nanocomposite Ti-B-N and Ti-B-C coatings deposited using different ion bombardment conditions. As a result of the difficult determination of the exact onset temperature for oxidation from dynamical TGA, the temperature at which the specific mass gain yields a value of 0.1 mg cm^{-2} for Ti-B-N and

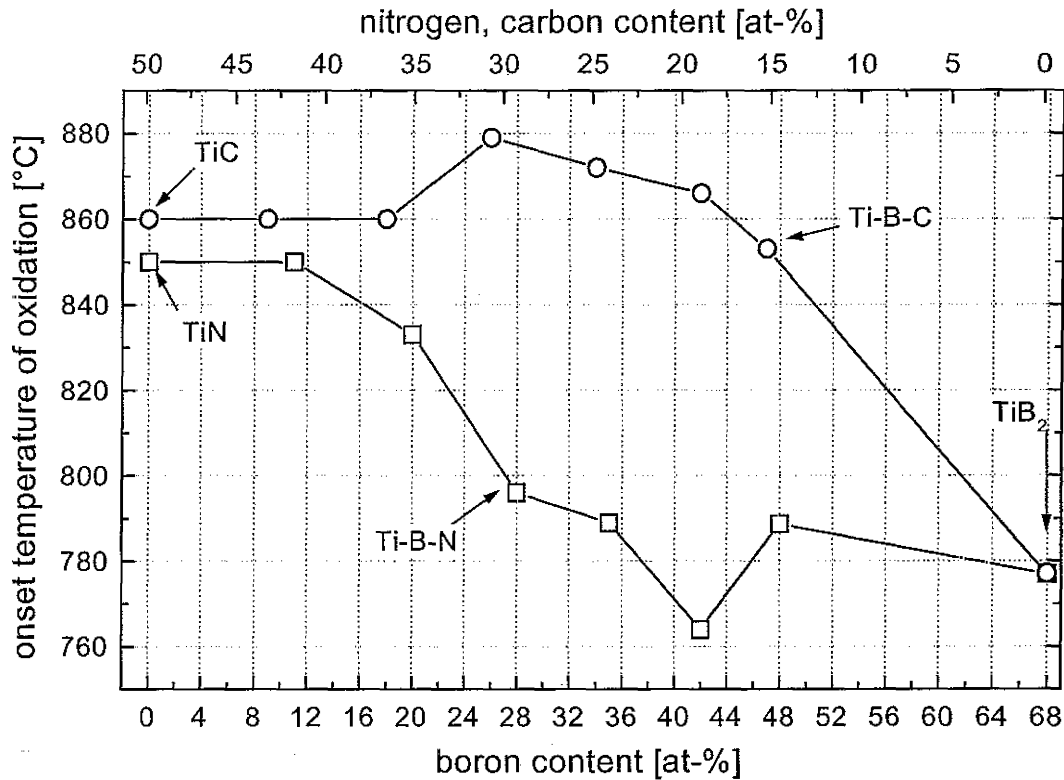


Figure 11. Onset temperature of oxidation for Ti-B-N and Ti-B-C coatings as a function of their chemical composition.

Ti-B-C overall coated steel discs was chosen for the description of the oxidation threshold. Fig. 11 shows this temperature of oxidation as a function of the chemical composition for Ti-B-N and Ti-B-C.

The oxidation temperatures for Ti-B-N coatings seem to be mainly dominated by their chemical composition, whereas Ti-B-C coatings having nearly the same amount of TiB_2 and TiC phases show higher oxidation temperatures than the single phase coatings TiB_2 and TiC . This behavior corresponds also to the findings during recrystallization of these nanocomposite coatings which showed a chemical composition dominated dependence of T_{rex} for Ti-B-N but not for Ti-B-C. SEM fracture cross sections after dynamical TGA in oxidizing atmosphere up to $900^\circ C$ clearly show the formation of different diffusion zones, due to the ion-diffusion of Ti, Fe and O. The oxidation products were characterized by means of XRD and energy dispersive spectroscopy (EDS) to be TiO_2 and Ti_3O_5 . Compared to oxidized CrN coatings [102], the oxidation products (TiO_2 and Ti_3O_5) of the Ti-B-N coatings (Fig. 12) are much more porous, even at the $100^\circ C$ lower oxidation temperature. Also no diffusion of Fe into the CrN coating was found during a TGA up to $1000^\circ C$. This is supposed to be mainly a reason of the lower amount of grain boundaries, which are favored paths for diffusion, since their grain sizes are more than ten times larger than those of the nanocomposite Ti-B-N coatings.

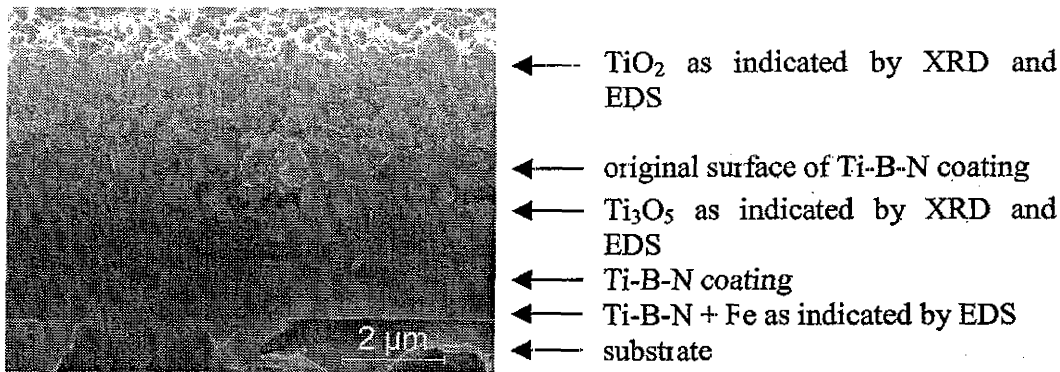


Figure 12. SEM fracture cross section of a TiB_{1.1}N_{0.5} coating after dynamical IGA in oxidizing atmosphere up to 900°C.

The oxidation products (TiO₂ and Ti₃O₅) of the Ti-B-N coatings do not act as a diffusion barrier due to their porous structure in contrast to the oxidation product of CrN. Therefore, no cavities or holes resulting from the accumulation of holes and possible released nitrogen are trapped behind the interface coating/oxide as it is valid for CrN [102]. Although the onset temperature of oxidation for Ti-B-N and Cr-N coatings are comparable, the oxidation product of the Cr-N coatings (Cr₂O₃) protects the nitrides much more effectively from a further oxidation attack than those of Ti-B-N. This behavior can clearly be seen from the comparison of the TGA curves of a CrN and the Ti-B-N coatings (Fig. 13).

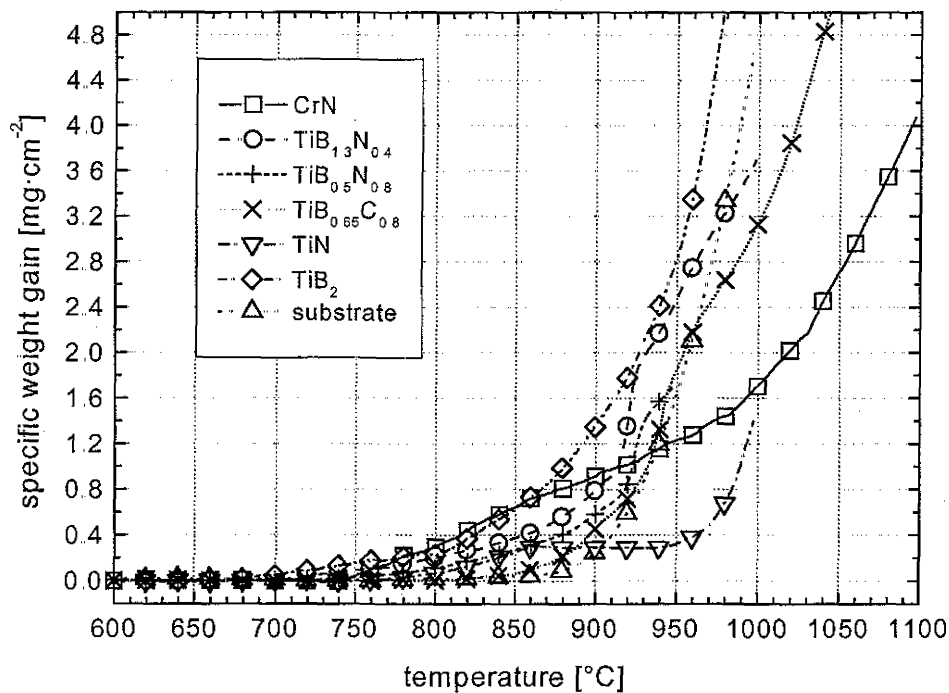


Figure 13. Dynamical IGA of Ti-B-N coatings compared to their single phase coatings (TiN and TiB₂), TiB_{0.65}C_{0.8} and CrN and the substrate used.

Fig. 13 shows as it can be seen from Fig. 11 that there is a slight increase in the oxidation threshold for the nanocomposite Ti-B-N coatings containing higher nitrogen contents. For all coatings except the CrN one, there is a rapid oxidation at temperatures higher than 950°C. This is mainly caused by breakaway oxidation, which is a result of cracks in the protecting oxide layer as discussed in ref. [102] for Cr-N coatings. This can be seen from the pronounced increase of the slope of the oxidation curves. Therefore, and as a consequence of a porous oxidation product which is valid for the Ti-B-N coatings (Fig. 12), there is almost no protection of the coatings by their oxide layers. This causes a rapid oxidation of the coatings (increasing ion diffusion of Ti and O) until they are completely dissolved. Consequently, their oxidation curves tend to be similar to that of the uncoated substrate. Ti-B-C coatings show similar oxidation curves during dynamical TGA (Fig. 13). Also their oxide layers show a comparable porous microstructure as those of Ti-B-N. TiN seems to have the most pronounced protective oxide layer on top of the coating up to a temperature of 950°C. But at higher temperatures also this coating shows an enhanced oxidation increase due to the breakaway oxidation. The very dense microstructure of the oxide layer on top of the CrN coatings [102] protects them from an increased oxidation attack even at temperatures higher than 950°C. Consequently, CrN shows the highest oxidation resistance, although their oxidation threshold (onset temperature of oxidation) is comparable to those of the other coatings.

5. Summary and conclusions

The motivation for the work described here has been the desire to understand mechanical properties and thermal stability of PVD hard coatings. It has been shown, that the interrelationship between deposition conditions, structure and mechanical properties and thermal stability of different hard coatings can be interpreted and understood in detail. This was done using internal growth-related deposition parameters for PVD processes, as well as the fundamental rules of materials science. It was found that the microhardness of single phase coatings like TiN and CrN follow the Hall-Petch relationship, or increase with increasing compressive stresses. The Young's modulus of the coatings could be reduced distinctly, just by decreasing the total working gas pressure, whereas their hardness remained nearly unaffected. The thermal stability of the different kind of point and line defects generated during the deposition process were investigated using biaxial stress temperature measurements during annealing. The main driving forces for the recovery processes are the temperature and the stresses within the coatings. Therefore, a linear dependence of the total amount of recovery effects, occurring during a thermal treatment, on the biaxial stresses of the coatings in the as-deposited state was found. The recrystallization behavior of nanocomposite TiN-TiB₂ and TiC-TiB₂ coatings could be investigated by DSC measurements. The onset temperature for recrystallization could be obtained by an exothermic peak during the DSC measurements up to 1400°C. This exothermic peak belong to a heat flow from the sample due to a reduction of the interfacial energy (i.e. grain growth). Using thermogravimetric analyses, the oxidation behavior of the coatings was investigated. It was found that Cr-N coatings which showed the lowest oxidation threshold have also the highest durability. This is the result of an extremely dense oxide-layer on top of the Cr-N coating, which prevents the coating from a further oxidation attack. The findings of the

work can be used as an important basis for further optimization of PVD processes and hard coatings.

Acknowledgements

Financial support of this work by the Technologie Impulse GmbH in the frame of the K-plus competence center program is highly acknowledged. The authors are grateful to Prof. J. Musil, Dr. H. Hrubý, Dr. P. Zeman, F. Kunc and H. Zeman (Department of Physics, University of West Bohemia, Plzen, Czech Republic) for microhardness measurements and valuable discussions. Furthermore, the authors' thanks are due to G. Tischler and H. Willmann for their excellent work on Cr-N and Ti-B-N coatings, respectively.

References

1. Schintlmeister, W., and Pacher, O. 1975, *J. Vac. Sci. Technol. A*, 12, 743.
2. Münz, W.-D. 1986, *J. Vac. Sci. Technol. A*, 4, 2717.
3. McIntyre, D., Greene, J.E., Håkansson, G., Sundgren, J.-E., and Münz, W.-D. 1990, *J. Appl. Phys.*, 67, 1542.
4. Smith, I.J., Münz, W.-D., Donohue, L.A., Petrov, I., and Greene, J.E. 1998, *Surf. Engin.*, 14, 37.
5. Donohue, L.A., Lewis, D.B., Münz, W.-D., Stack, M.M., Lyon, S.B., Wang, H.-W., and Rafaja, D. 1999, *Vacuum* 55, 109.
6. Navinšek, B., Panjan, P., and Milošev, I. 1997, *Surf. Coat. Technol.*, 97, 182.
7. Grill, A. 1999, *Diam. Relat. Mater.*, 8, 428.
8. Faure, C., Hänni, W., Schmutz, C.J., and Gervanoni, M. 1999, *Diam. Relat. Mater.*, 8, 830.
9. Mirkarimi, P.B., McCarty, K.F., and Medlin, D.L. 1997, *Mater. Sci. Engin. Reports*, 21, 47.
10. Schneider, J.M., Sproul, W.D., and Matthews, A. 1998, *Surf. Coat. Technol.*, 98, 1473.
11. Schintlmeister, W., Wallgram, W., Kanz, J., and Gigl, K. 1984, *Wear*, 100, 153.
12. Vepřek, S. 1999, *J. Vac. Sci. Technol. A*, 17, 2401.
13. Holleck, H., and Schier, V. 1995, *Surf. Coat. Technol.*, 76-77, 328.
14. Voevodin, A.A., O'Neill, J.P., and Zabinski, J.S. 1999, *Surf. Coat. Technol.*, 116-119, 36.
15. Gilmore, R., Baker, M.A., Gibson, P.N., Gissler, W., Stoiber, M., Losbichler, P., and Mitterer, C. 1998, *Surf. Coat. Technol.*, 108-109, 345.
16. Quinto, D. I. 1996, *Int. J. Refract. Metals Hard Mater.*, 14, 7.
17. Mattox, D.M. 2000, *Surf. Coat. Technol.*, 133-134, 517.
18. Schneider, J.M., Rohde, S., Sproul, W.D., and Matthews, A. 2000, *J. Phys. D: Appl. Phys.*, 33, R173.
19. Konuma, M. 1992, *Film Deposition by Plasma Techniques*, Springer, Berlin Heidelberg.
20. Losbichler, P., and Mitterer, C. 1997, *Surf. Coat. Technol.*, 97, 568.
21. Paturaud, C., Farges, G., Sainte Catherine, M.C., and Machet, J. 1998, *Surf. Coat. Technol.*, 98, 1257.
22. Thornton, J.A. 1974, *J. Vac. Sci. Technol.*, 11(4), 666.
23. Messier, R., Giri, A.P., and Roy, R.A. 1984, *J. Vac. Sci. Technol. A*, 2(2), 500.
24. Mattox, D.M. 1989, *J. Vac. Sci. Technol. A*, 7(3), 1105.
25. Mayrhofer, P.H., Kunc, F., Musil, J., and Mitterer, C. 2002, *Thin Solid Films*, accepted.
26. Musil, J. 2000, *Surf. Coat. Technol.*, 125, 322.
27. Jehn, H.A. 1992, *Advanced Techniques for Surface Engineering*, Gissler, W., Jehn, H.A. (Eds.), Brussels, 5.
28. Losbichler, P. 1998, *Ultraharte PVD-Schichten im System Ti-B-N*, PhD Thesis, University of Leoben.

29. Losbichler, P., Mitterer, C., Gibson, P.N., Gissler, W., Hofer, F., and Warbichler, P. 1997, *Surf. Coat. Technol.*, 94/95, 297.
30. Mayrhofer, P.H., and Mitterer, C. 2000, *Surf. Coat. Technol.*, 133-134, 131.
31. Hultman, L., Münz, W.-D., Musil, J., Kadlec, S., Petrov, I., and Greene, J.E. 1991, *J. Vac. Sci. Technol. A*, 9(3), 434.
32. Pelleg, J., Zevin, L.Z., Lungo, S., and Croitoru, N. 1991, *Thin Solid Films*, 197, 117.
33. Hultmann, L., Sundgren, J.-E., Markert, L.C., and Greene, J.E. 1989, *J. Vac. Sci. Technol. A*, 7(3), 1187.
34. Kodambaka, S., Petrova, V., Vailionis, A., Desjardinis, P., Cahill, D.G., Petrov, I., and Greene, J.E. 2001, *Thin Solid Films*, 392, 164.
35. Petrov, I., Hultman, L., Helmersson, U., Sundgren, J.-E., and Greene, J.E. 1989, *Thin Solid Films*, 169, 299.
36. Adibi, F., Petrov, I., Greene, J.E., Hultman, L., and Sundgren, J.-E. 1993, *J. Appl. Phys.*, 73(12), 8580.
37. Mitterer, C., Mayrhofer, P.H., Kelesoglu, E., Wiedemann, R., and Oettel, H. 1999, *Z. Metallkd.*, 90, 8.
38. Oettel, H., and Klimanek, P. 1998, *Materials Science Forum*, 273-275, 55.
39. Piot, O., Gautier, C., and Machet, J. 1997, *Surf. Coat. Technol.*, 94-95, 409.
40. Petrov, I., Adibi, F., Greene, J.E., Hultman, L., and Sundgren, J.-E. 1993, *Appl. Phys. Letters*, 63, 36.
41. Kadlec, S., Musil, J., Münz, W.-D., Håkanson, G., and Sundgren, J.E. 1989, *Surf. Coat. Technol.*, 39/40, 487.
42. Quaeysaegens, C., Knuyt, G., D'Haen, J., and Stals, L.M. 1995, *Thin Solid Films*, 258, 170.
43. Knuyt, G., Quaeysaegens, C., D'Haen, J., and Stals, L.M. 1995, *Surf. Coat. Technol.*, 76/77, 311.
44. Arzt, E. 1998, *Acta Mater.*, 46, 5611.
45. Hall, E.O. 1951, *Proc. Phys. Soc. B*, 64, 747.
46. Petch, N.J. 1953, *Journal of the Iron and Steel Institute*, 174, 25.
47. Kim, H.S. 1998, *Scripta Mater.*, 39, 1057.
48. Mayrhofer, P.H., Tischler, G., and Mitterer, C. 2001, *Surf. Coat. Technol.*, 142-144, 78.
49. Shioz, J., Vegge, T., DiTolla, F.D., and Jacobson, K.W. 1999, *Phys. Rev. B*, 60, 11971.
50. Mayrhofer, P.H. 2001, *Material Science Aspects of Nanocrystalline PVD Hard Coatings*, PhD Thesis, University of Leoben.
51. Sproul, W.D. 1996, *Surf. Coat. Technol.*, 86-87, 170.
52. Helmersson, U., Todorova, S., Barnett, S.A., Sundgren, J.-E., Markert, L.C., and Greene, J.E. 1987, *J. Appl. Phys.*, 62, 481.
53. Chu, X., Wong, M.S., Sproul, W.D., Rohde, S.L., and Barnett, S.A. 1992, *J. Vac. Sci. Technol. A*, 10, 1604.
54. Chu, X., and Barnett, S.A. 1995, *J. Appl. Phys.*, 77, 4403.
55. Hovsepian, P.Eh., Lewis, D.B., and Münz, W.-D. 2000, *Surf. Coat. Technol.*, 133-134, 166.
56. Vepřek, S., and Reiprich, S. 1995, *Thin Solid Films*, 268, 64.
57. Niederhofer, A., Nesládek, P., Männling, H.-D., Moto, K., Vepřek, S., and Jilek, M. 1999, *Surf. Coat. Technol.* 120-121, 173.
58. Vepřek, S., Niederhofer, A., Moto, K., Bolom, I., Männling, H.D., Nesládek, P., Dollinger, G., and Bergmaier, A. 2000, *Surf. Coat. Technol.*, 133-134, 152.
59. Vepřek, S. 1997, *Surf. Coat. Technol.*, 97, 15.
60. Mitterer, C., Mayrhofer, P.H., Beschliesser, M., Losbichler, P., Warbichler, P., Hofer, F., Gibson, P.N., Gissler, W., Hrubý, H., Musil, J., and Vlček, J. 1999, *Surf. Coat. Technol.*, 120-121, 405.
61. Zeman, P., Čerstvý, R., Mayrhofer, P.H., Mitterer, C., and Musil, J. 2000, *Mater. Sci. Engin. A*, 289, 189.
62. Leyland, A., and Matthews, A. 2000, *Wear*, 246, 1.

63. Mitterer, C., Losbichler, P., Hofer, F., Warbichler, P., Gibson, P.N., and Gissler, W. 1998, *Vacuum*, 50, 313.
64. Musil, J., Viček, J., Zeman, P., Setsuhara, Y., Miyake, S., Komuna, S., Yabato, K., Saito, H., Kumagai, M., and Mitterer, C. 2002, *Jap. J. Appl. Physics*, submitted.
65. Klug, H.P., and Alexander, L.E. 1974, *X-Ray Diffraction Procedures*, John Wiley & Sons Inc., New York.
66. De Keijser, Th.H., Langford, J.I., Mettemeijer, E.J., and Vogels, A.B.P. 1982, *J. Appl. Cryst.*, 15, 308.
67. Langford, J.I. 1978, *J. Appl. Cryst.*, 11, 10.
68. Schiøtz, J., Di Tolla, F.D., and Jacobsen, K.W. 1998, *Nature*, 391, 561.
69. Vepřek, S., Nesládek, P., Niederhofer, A., Glatz, F., Jilek, M., and Sima, M. 1998, *Surf. Coat. Technol.*, 108/109, 138.
70. Matthews, A. 1984, The value of deposition processes for industrial tools, *Proceedings of the 1st Conference on Materials Engineering*, Institution of Metallurgists, University of Leeds, 175.
71. Tsui, I.Y., Pharr, G.M., Oliver, W.C., Bhatia, C.S., White, R.L., Anders, S., Anders, A., and Brown, I.G. 1995, *Mater. Res. Soc. Symp. Proc.*, 383, 447.
72. Pharr, G.M. 1998, *Mater. Sci. Eng. A*, 253, 1/2, 151.
73. Haasen, P. 1978, *Physical Metallurgy*, Cambridge University Press, London.
74. Mitterer, C., Holler, F., Üstel, F., and Heim, D. 2000, *Surf. Coat. Technol.*, 125, 233.
75. Verhoeven, J.D. 1975, *Fundamentals of Physical Metallurgy*, Wiley, New York.
76. Nix, W.D. 1989, *Metall. Trans. A*, 20, 2217.
77. Hultman, L. 2000, *Vacuum*, 57, 1.
78. Barrett, C.S., and Massalski, I.B. 1980, *Structure of Metals*, Pergamon Press, Oxford.
79. Guy, A.G. 1983, *Metallkunde für Ingenieure*, Akademische Verlagsgesellschaft, Wiesbaden.
80. Humphreys, F.J., and Hatherly, M. 1995, *Recrystallization and Related Annealing Phenomena*, Elsevier Science, Oxford.
81. Novikov, V. 1997, *Grain Growth and Control of Microstructure and Texture in Polycrystalline Materials*, CRC Press, Boca Raton.
82. Humphreys, F.J. 1998, *Proceedings of Third International Conference on Grain Growth*. *Miner Metals & Mater. Soc.*, Warrendale, 13.
83. Haessner, F. 1978, *Recrystallization of Metallic Materials*, Haessner, F. (Ed.), Riederer-Verlag, Stuttgart, 1.
84. Machlin, E.S. 1995, *Materials Science in Microelectronics*, Giro Press, New York.
85. Oettel, H., and Wiedemann, R., 1995, *Surf. Coat. Technol.*, 76-77, 265.
86. Rossnagel, S.M. 1989, *J. Vac. Sci. Technol. A*, 7(3), 1025.
87. Schatt, W., and Worch, H. 1996, *Werkstoffwissenschaft*, Deutscher Verlag für Grundstoffindustrie, Stuttgart.
88. Hultman, L., Engström, C., and Odén, M. 2000, *Surf. Coat. Technol.*, 133-134, 227.
89. Suryanarayana, C. 1995, *International Materials Reviews*, 40(2), 41.
90. Detert, K. 1978, *Recrystallization of Metallic Materials*, Haessner, F. (Ed.), Riederer-Verlag, Stuttgart, 97.
91. Stüwe, H.P. 1978, *Recrystallization of Metallic Materials*, Haessner, F. (Ed.), Riederer-Verlag, Stuttgart, 11.
92. Hornbogen, E., and Köster, U. 1978, *Recrystallization of Metallic Materials*, Haessner, F. (Ed.), Riederer-Verlag, Stuttgart, 159.
93. Mitterer, C., Rauter, M., and Rödhammer, P. 1990, *Surf. Coat. Technol.*, 41, 351.
94. Kissinger, H.E. 1957, *Anal. Chem.*, 29, 1702.
95. Lu, K., Dong, Z.F., Bakonyi, I., and Cziraki, A. 1995, *Acta Metal Mater.*, 43(7), 2641.
96. Trethewey, K.R., and Chamberlain, J. 1995, *Corrosion for Science and Engineering*, 2nd Edition, Longman Group Ltd., Singapore.
97. Evans, U.R. 1968, *The Corrosion and Oxidation of Metals*, Arnold, London.

-
98. Grabke, G.J., and Schütze, M. 1998, Oxidation of Intermetallics, Grabke, G.J. (Ed), VCH Verlag, Weinheim.
 99. West, J.M. 1980, Basic Corrosion and Oxidation, Ellis Horwood, Chichester.
 100. Fromm, E. 1998, Kinetics of Metal-Gas Interactions at Low Temperatures, Springer Verlag, Berlin.
 101. Hauffe, K. 1965, Oxidation of Metals, Plenum Press, New York.
 102. Mayrhofer, P.H., Willmann, H., and Mitterer, C. 2001, Surf. Coat. Technol., 146-147 222.